Lab on a Chip

Actuated 3D microgels for single cell mechanobiology

Journal:	*Lab on a Chip*
Manuscript ID	LC-ART-03-2022-000203.R1
Article Type:	Paper
Date Submitted by the Author:	01-Apr-2022
Complete List of Authors:	Özkale, Berna; Technical University of Munich, Lou, Junzhe ; Harvard University, School of Applied Sciences and Engineering Ozelci, Ece; Ecole Polytechnique Federale de Lausanne, STI IGM Elosegui-Artola, Alberto; Harvard University, School of Applied Sciences and Engineering Tringides, Christina; Harvard University, School of Applied Sciences and Engineering Mao, Angelo ; Harvard University Wyss Institute for Biologically Inspired Engineering, Sakar, Mahmut Selman; Ecole Polytechnique Federale de Lausanne, Mechanical Engineering Mooney, David; Harvard University, John A. Paulson School of Engineering and Applied Sciences

ARTICLE

Actuated 3D microgels for single cell mechanobiology

Berna Özkale,[ab] Junzhe Lou,[ab] Ece Özelçi,[c] Alberto Elosegui-Artola,[ab] Christina M. Tringides,[ab] Angelo S. Mao,[ab] Mahmut Selman Sakar*[c] and David J. Mooney*[ab]

Received 00th January 20xx,
Accepted 00th January 20xx

DOI: 10.1039/x0xx00000x

We present a new cell culture technology for large-scale mechanobiology studies capable of generating and applying optically controlled uniform compression on single cells in 3D. Mesenchymal stem cells (MSCs) are individually encapsulated inside an optically triggered nanoactuator-alginate hybrid biomaterial using microfluidics, and the encapsulating network isotropically compresses the cell upon activation by light. The favorable biomolecular properties of alginate allow cell culture in vitro up to a week. The mechanically active microgels are capable of generating up to 15% compressive strain and forces reaching 400 nN. As a proof of concept, we demonstrate the use of the mechanically active cell culture system in mechanobiology by subjecting singly encapsulated MSCs to optically generated isotropic compression and monitoring changes in intracellular calcium intensity.

Introduction

Single cell screening technologies have emerged as powerful tools for capturing variations in gene expression and protein content within populations of cells. Mapping the entire -omics information has the potential to reveal the role of heterogeneity in cellular functions with relevance to cancer, development, and regeneration.[1-4] However, most attention to date has been directed at biomolecular profiling, although the significance of mechanotransduction on cell behavior has become evident with the introduction of micromanipulation methods including micropipette aspiration, magnetic tweezers, atomic force microscopy, and optical tweezers.[5-12] New strategies for large-scale, single cell biomechanical screening may provide unique opportunities to study how individual cells sense, interpret, and transmit forces.

Encapsulation of cells in synthetic three-dimensional (3D) extracellular matrices (ECM) has emerged as an instrumental technique to study the mechanics of cell-ECM interactions. Combined with microfluidics technology, millions of microtissues can be produced with one to a few cells packaged inside individual hydrogels in minutes. Rapid generation of distinct 3D micromatrices using microfluidics allows fast production of many independent samples with minimal variances between biomaterial scaffolds, while allowing better diffusion of nutrients to encapsulated cells compared to bulk hydrogels.[13] Moreover, microencapsulated cells belonging to different groups can be used to assemble tissue-like constructs that can be used to simulate complex in vivo processes under simplified conditions.[14] We have recently introduced a method for the deterministic encapsulation of single cells in small alginate microgels.[15,16] The naturally-derived biopolymer alginate has tunable biomolecular and mechanical properties, making it suitable for culturing a wide variety of cell types.[17-21] Alginate can be chemically functionalized with integrin binding RGD peptides to enable cell adhesion and varying cell adhesion ligand density in 3D matrices was recently shown to influence MSC differentiation.[21] Moreover, alginate matrices are compatible with molecular tension sensors, enabling precise quantification of cell generated forces in situ.[20] However, externally controlled actuation techniques that are capable of manipulating stress and strain within alginate matrices are limited.

While micromanipulation strategies relying on nanotechnology, nanomanipulators, microfluidics, and stretchable elastomers have proven to be powerful tools for the application of externally regulated forces and stresses on single cells, these methods typically suffer from spatial limitations in the direction of applied force.[22] Moreover, they often require planar cell culture conditions and fall short in recreating biologically relevant 3D environments. The introduction of plasmonic and magnetic nanotransducers into highly deformable hydrogels enabled actuatable soft substrates[23,24,25] as well as 3D structures[26,27] that can be interfaced with living cells. The rotation of electroplated magnetic rods and laser-cut sheets using externally applied homogenous magnetic fields generated controllable torques within fibrillar matrices.[28,29] These examples highlight the potential of mechanically active cell culture systems while indicating a clear need for further development towards single cell technologies.

In this work, we present a mechanically active cell culture platform consisting of optically powered and controlled nanoactuators that are seamlessly integrated into single cell-

---

[a] *Harvard John A. Paulson School of Engineering and Applied Sciences, Harvard University, Cambridge, MA, 02138, USA*
E-mail: selman.sakar@epfl.ch, mooneyd@seas.harvard.edu
[b] *Wyss Institute for Biologically Inspired Engineering, Cambridge, MA, 02138, USA*
[c] *Institute of Mechanical Engineering and Institute of Bioengineering, Ecole Polytechnique Fédérale de Lausanne (EPFL), CH-1015, Lausanne, Switzerland*

† Footnotes relating to the title and/or authors should appear here.

Electronic Supplementary Information (ESI) available. See DOI: 10.1039/x0xx00000x

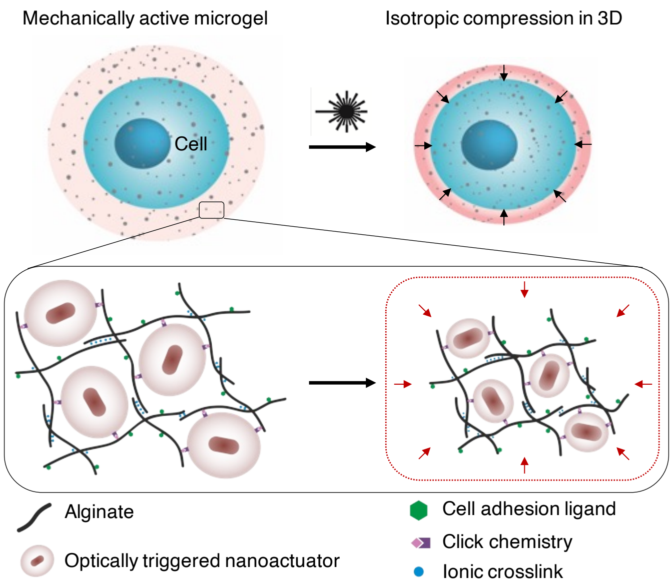

Fig. 1 Schematic description of the mechanically active single cell culture platform. A single cell encapsulated microgel contracts when stimulated by NIR light and the encapsulating hydrogel-nanoactuator network exerts isotropic compression on the cell in all directions. Mechanical coupling between alginate and optically triggered nanoactuators via click chemistry allow force transmission through the network. Alginate is modified with cell adhesion ligands (RGD) to promote cell-ECM binding and the hydrogel is ionically crosslinked.

laden alginate microgels using microfluidics (Fig. 1). The synergistic effect between the surface plasmon resonance of gold nanorods and thermally activated reversible shrinkage of the polymer poly(N-isopropylmethacrylamide) (pNIPMAM) leads to nanoscale actuators capable of generating tens of pN.[23] A single microactuator consisting of a network of optically controlled nanoactuators without encapsulated cells can generate compressive forces as high as 10.3 μN.[26] Alginate was selected as the cell encapsulating matrix because of its favorable biomolecular properties, namely ease of functionalization with cell adhesion ligands, biorthogonal crosslinking, biological inertness, and tunable mechanical properties.[17] We find that covalent crosslinking between these two components provides efficient force transmission throughout the active biomaterial network. Cells encapsulated within this material experience isotropic compression as the microgel shrinks under near-infrared (NIR) light. We chose photothermal actuation to drive compression in actuated microgels as optical control methods typically allow better spatial resolution and do not suffer from power attenuation with increasing distance from the source. As a proof of concept, we show that isotropic compression triggers reversible, mechanosensitive intracellular calcium signaling in single MSCs. The actuated microgels possess the unique capability of applying uniform and isotropic compressive stresses within a mechanically tunable 3D substrate. The magnitude and frequency of loading can be tuned on demand and multiple single cells can be stimulated in sequence within the same workspace. Moreover, this approach offers the possibility to study cellular and nuclear dynamics in real-time owing to the nano-scale reversible strain induced on the encapsulated cells. Taken together, our mechanically active single cell culture and manipulation system enables a new class of biomechanical studies at the single cell level.

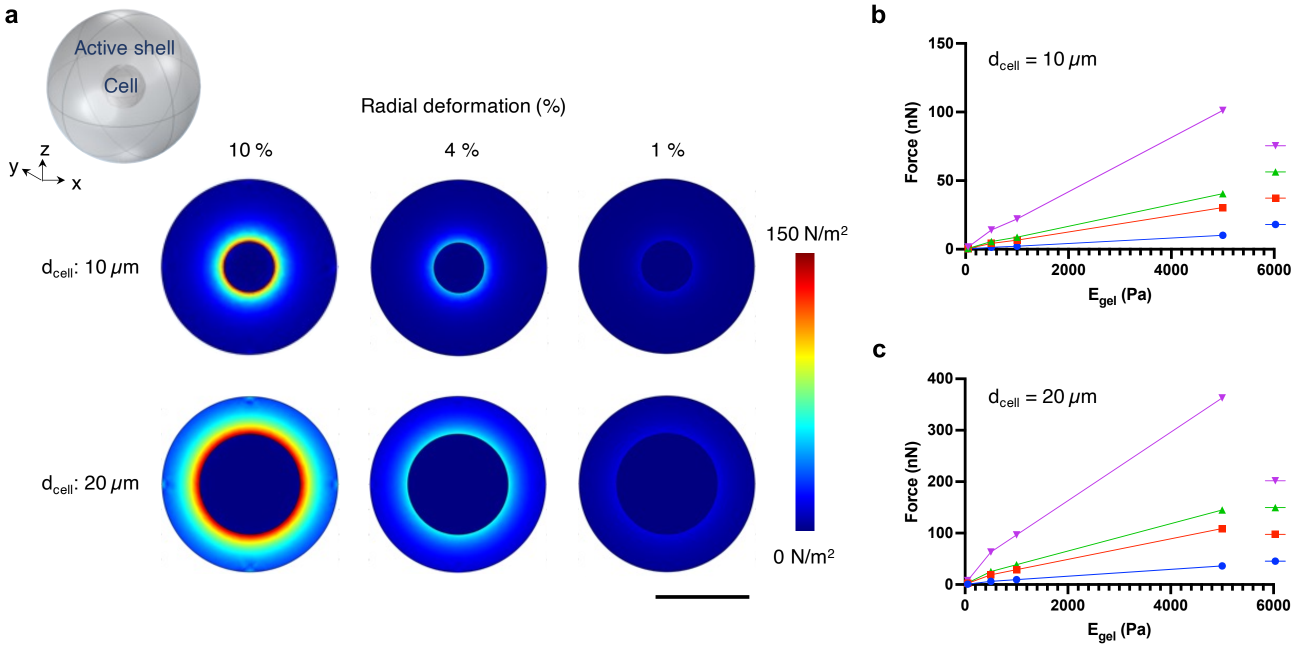

Fig. 2 Theoretical force estimation in mechanically active microgels. (a) Cross-sectional stress maps are given for three radial strain cases (10%, 4%, and 1%) and two cell sizes (10 and 20 μm). For all cases overall microgel size was 35 μm and Young's moduli of the microgel and the cell was 1 kPa and 3 kPa, respectively. Scale bar: 20 μm. The influence of encapsulating hydrogel stiffness and radial deformation on total generated force are plotted for cell sizes of (b) 10 μm and (c) 20 μm.

Results and discussion

Computational modeling to estimate applied forces

To estimate the forces generated in this cell culture system, we simulated stress distribution at the cell-biomaterial interface using finite-element modeling (Fig. 2). The active shell consisted of nanoscale actuators dispersed in a network of ionically crosslinked alginate which we previously showed behaves as a linearly elastic solid under compression for up to 15% strain.[30] The thermoresponsive component of the nanoactuators, poly(*N*-isopropylacrylamide), has also been reported to behave as linearly elastic solids within the same compressive strain values.[31,32] In our experiments, we actuated the shell for short time periods on the order of a few seconds and in a non-repetitive fashion. Under these loading conditions and material properties, the non-linear effects were not expected to significantly affect the calculations. Therefore both the cell and the contracting active shell were modeled as linearly elastic solids.

We applied the experimentally measured isotropic displacements of actuated gels uniformly as boundary conditions in the simulations (Fig. 2a). We generated stress maps by integrating von Misses stresses over the ball surface that represents the encapsulated cell for three shell contraction cases corresponding to low (1%), medium (4%), and high strain (10%). Generated stress increased by an order of magnitude as radial strain increased from 1% to 10%, and reached a maximum of 150 Pa for 1 kPa shell stiffness (Fig. 2a). This corresponded to a total force of 22 nN and 97 nN for a cell diameter of 10 µm and 20 µm, respectively (Fig. 2b, c). Increasing the Young's modulus of the shell to 5 kPa raised the total force to 400 nN (Fig. 2c, Fig. S1). These calculations indicate that the proposed active microgel system could deliver biologically relevant forces even at medium strain (4%). Previous work has shown that mechanobiological responses such as integrin activation, focal adhesion reinforcement, and nuclear shuttling of transcription factors require the application of forces within a range of tens of pN to nN.[34]

Microfluidic cell encapsulation in active microgels

Next, active microgels were fabricated using a combination of synthetic chemistry and microfluidics. We chose alginate as the static ECM component due to its compatibility with high-throughput microfluidic synthesis and tunable chemical as well as mechanical properties allowing its use as an artificial ECM for a wide variety of cells. On the other hand, pNIPMAM was selected to construct the optically triggered nanoactuators because of its high swelling ratio, excellent thermal response, and repeatable actuation capacity.[34] Moreover, these nanoactuators have been successfully used for mechanobiology research before.[23] Our actuation approach is compatible with other hydrogel materials provided that the nanoactuators are firmly coupled to the backbone of the biopolymer. A variety of functional groups (e.g. amine groups) can be added to the surface of the nanoactuators during the synthesis process to facilitate chemical crosslinking.[26,27]

Optically controlled nanoactuators were synthesized via seed-mediated gold nanorod growth and *in situ* free-radical polymerization of pNIPMAM, following a published protocol.[26] The gold nanorod core – pNIPMAM nanoparticles (Fig. 3a, Fig.

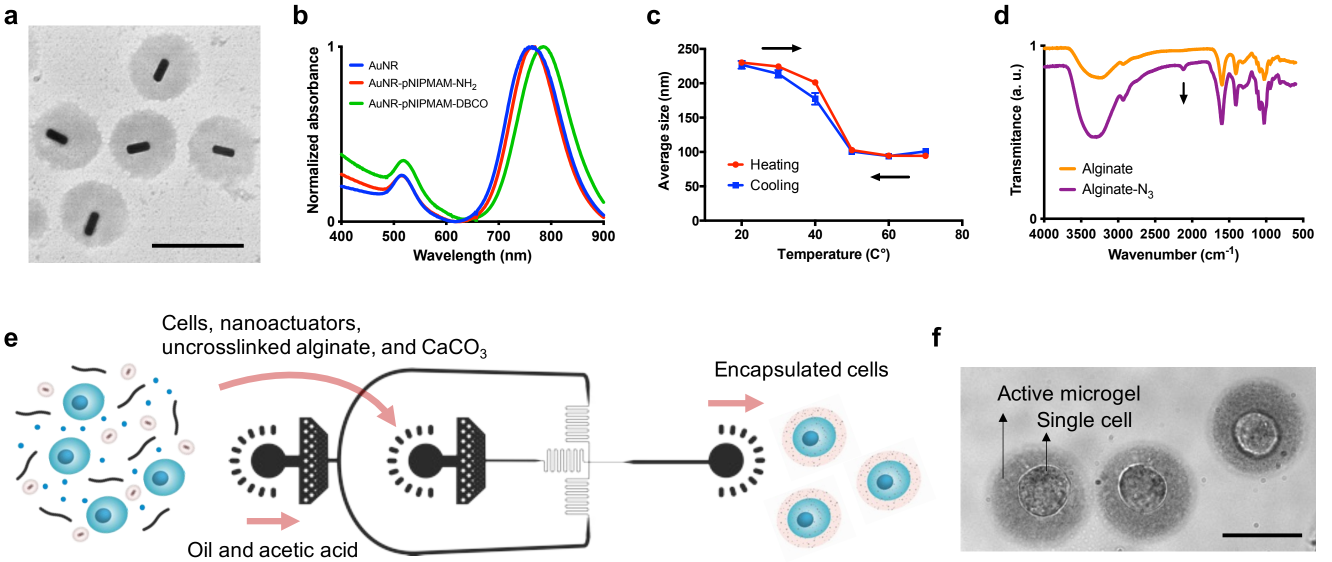

Fig. 3 Nanoactuator synthesis and mechanically active microgel fabrication. (a) TEM image of nanoactuators. Gold nanorods appear dark surrounded by a bright appearing polymer shell. Scale bar: 500 nm (b) UV-vis spectra of gold nanorods (AuNRs) and gold nanorod-pNIPMAM nanoactuators functionalized with either amines or DBCO. (c) Temperature induced changes in nanoactuator hydrodynamic size. Nanoactuators in an aqueous environment reversibly shrink and revert to original size when heated and cooled respectively. (d) FTIR spectra comparing unfunctionalized and azide modified alginate where arrow points to azide functional groups. (e) Schematic representation of the microfluidic encapsulation process. A pre-gel mixture of cells, alginate, calcium carbonate nanoparticles, and nanoactuators is flown through a two-channel microfluidic device. The acetic acid in the oil phase dissolves calcium carbonate and crosslinks the cell encapsulating hydrogel network as microgel droplets are formed. (f) A bright-field image showing single cell encapsulating active microgels. Scale bar: 30 µm.

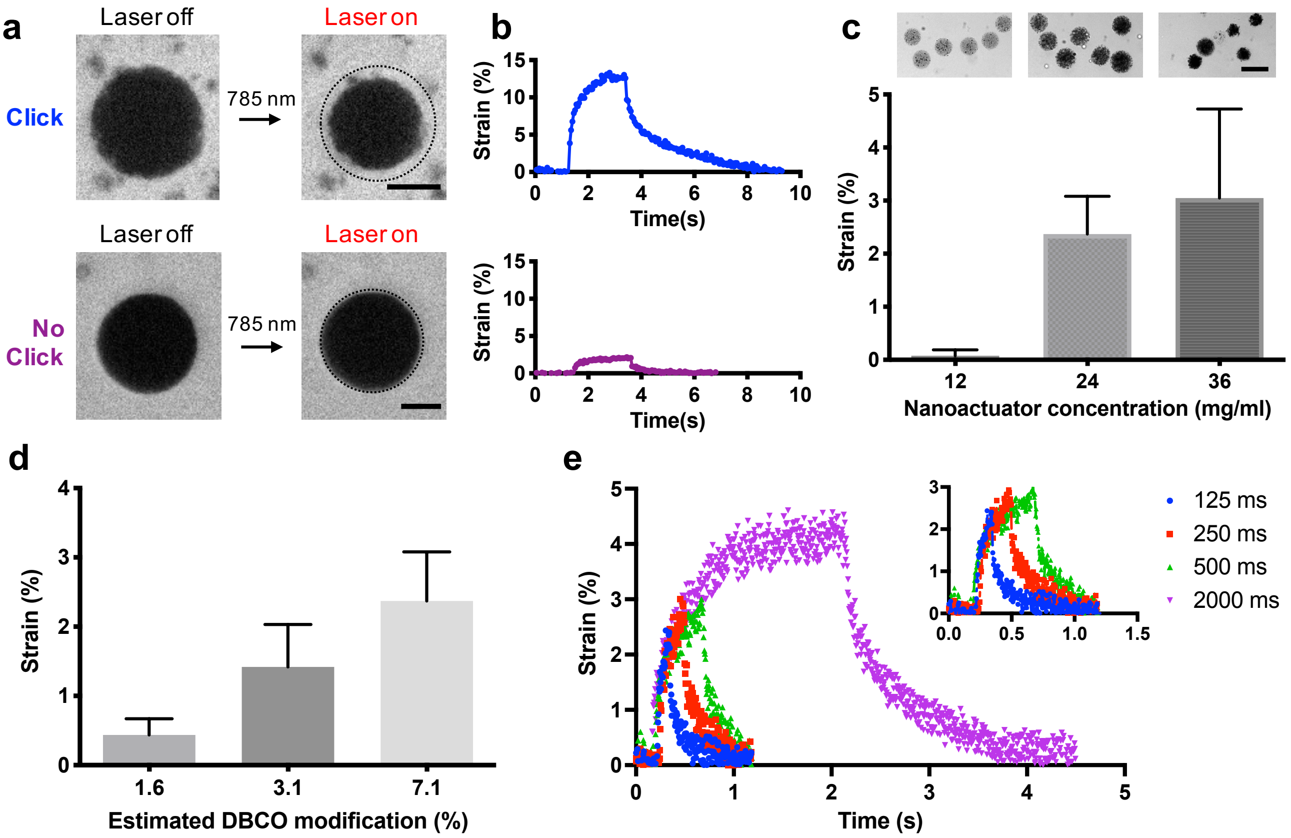

Fig. 4 Characterization and optimization of radial strain in mechanically active microgels. (a) Influence of covalent crosslinking between alginate and nanoactuators. Example of a click modified microgel actuator at high nanoparticle concentration (57 mg/ml) versus no click case (67 mg/ml) and (b) corresponding strain plots for a single actuation cycle with 2 seconds laser application (scale bar: 20 µm). Average strain was -15.5% +/- 7.6 (n=9) for click microgels and -3.3% +/- 1.4 (n=6) for the case without DBCO-azide click modification. The observed absolute radial displacement for the click and no click microgels was 10.6 µm and 1.1 µm respectively. Dotted lines show initial microactuator boundary before optical activation. (c) Influence of nanoactuator concentration on average radial strain in dynamic microgels and representative images of the corresponding conditions are shown (scale bar: 50 µm). Average strain for 12, 24, and 36 mg/ml are -0.074 +/- 0.11 (n=6), -2.37 +/- 0.71 (n=15), -3.05 +/- 1.68 (n=15), respectively. For all conditions microgels were actuated with a single laser pulse of 500 msec at 50 mW. Click modification is 1 mg/mg HP. (d) The effect of varying surface DBCO modification on nanoactuators in terms of strain generated when microgels are actuated at 50 mW for 500 msec. All conditions were fabricated with 24 mg/ml nanoactuator concentration. (e) Microactuator strain profile is tuned by changing the laser pulse on duration. Inset shows a close up of 125-500 msec pulse durations with corresponding deformation profiles.

S2) exhibited distinct optical properties at the NIR range (Fig. 3b), and underwent a 50% change in hydrodynamic size when thermally activated (Fig. 3c). A biocompatible and fast copper-free click chemistry based on dibenzocyclooctyne (DBCO) and azide was chosen to mechanically link the nanoactuators to the cell encapsulating network. The nanoactuator surface was decorated with DBCO by using the surface amine groups that were incorporated during the pNIPMAM polymerization step. While the polymer coating had negligible impact on the absorption spectrum, the modification of DBCO led to a significant shift in the peak from 770 nm to 785 nm (Fig. 3b) most likely due to the conjugated electronic structure of the DBCO (i.e. the large delocalized pi molecular orbitals).

Alginate was crosslinked by calcium ions to generate the hydrogel network and served as the cell encapsulation component of the active microgel. Azide moieties and RGD containing peptide (GGGGRGDSP) were conjugated to alginate via carbodiimide chemistry, which allowed conjugation with nanoactuators (Fig. 3d) and promoted cell-matrix adhesion through integrin binding (Fig. S3) respectively.

Active microgels were fabricated by flowing a pre-gel mixture of gold nanorod-pNIPMAM nanoparticles, alginate, and calcium carbonate nanoparticles through the microfluidic device (Fig. 3e), using a two-channel microfluidic encapsulation device.[15,16] The acetic acid in the surrounding oil phase diffused into the droplet and dissolved the calcium carbonate nanoparticles as droplets were formed. The released free calcium ions crosslinked the alginate while the DBCO-azide click reaction simultaneously coupled nanoactuators to alginate chains. MSCs were singly encapsulated within the active microgel network using this approach and the resulting 3D microniches were approximately 30 µm in size (Fig. 3f). For this purpose, cells were treated with calcium carbonate nanoparticles to adsorb the nanoparticles on the MSC surface. This additional step ensured high encapsulation efficiency, and significantly reduced the number of cell-free microgels.

Strain characterization in active microgels and bio-integration

Covalently crosslinked active microgels responded to 785 nm light with up to 15% radial strain, while those without click

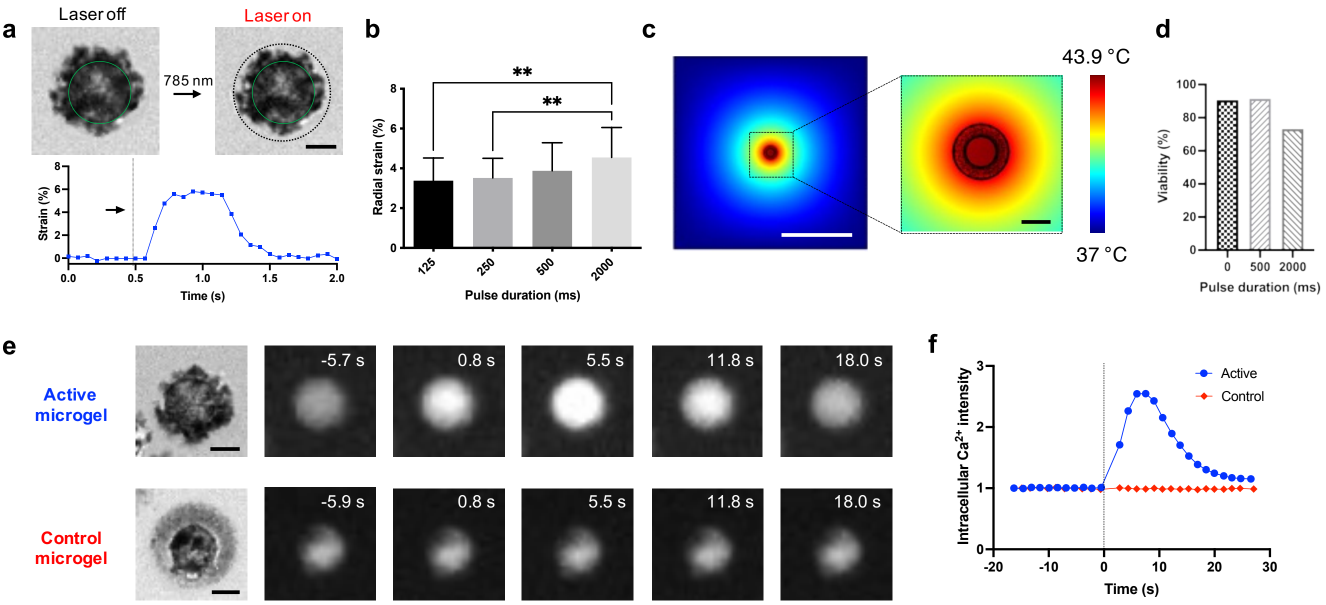

Fig. 5 Integration of mesenchymal stem cells in active microgels and Influence of isotropic compression on mechanochemical signaling in single cells. (a) Before and after actuation images of a cell encapsulated click microgel with the corresponding strain versus time curve, arrow shows the timepoint of actuation. A single pulse of 500 ms was applied (scale bars: 10 μm). The continuous green line indicates the cell outline in both images while the dotted black line shows the initial circumference of the active microgel. Active microgels were prepared using 18 mg/ml nanoactuator concentration with 7.1% DBCO modification. (b) Comparison of average radial strain in active microgels for 125 ms (n=22), 250 ms (n=54), 500 ms (n=50), and 2000 ms (n=34) pulse durations under 5.5 μW/μm2 laser power. ** indicates significant difference analyzed using one-way analysis of variance (ANOVA) followed by Šídák multiple comparison test, $p<0.05$ (c) Simulated heat maps (scale bars: 200 μm and 20 μm respectively). (d) MSC viability before and 24 hours after a single cycle of laser actuation for 500 and 2000 ms (0 ms (n=53), 500 ms (n=47), 2000 ms (n=41)). MSCs were encapsulated in control microgels which could be photothermally heated without exhibiting isotropic compression. (e) Series of images showing intracellular calcium intensity in active and control microgels (scale bars: 10 μm) and (f) corresponding plot presenting normalized intracellular calcium intensity over time. The radial strain in active microgels with 7.1% DBCO modification and control microgels without any DBCO was 6% and 1.3% respectively corresponding to estimated forces of 103 nN and 22 nN assuming 1 kPa Young's modulus.

modification exhibited 2% strain when actuated under the same laser intensity (Fig. 4). The maximum achievable force at microgel-cell interface under these strain conditions was estimated to be 1215 nN using click microgels which decreases substantially without covalent coupling to 162 nN for a 20 μm encapsulated cell. Here, radial strain referred to percentage change in microgel diameter and was calculated using planar brightfield images taken during laser *on* and *off* phases. Microgels returned to their initial size within 6 sec following laser activation, and actuation performance remained the same over 12 cycles (Fig. S4).

Despite the excellent deformation capabilities, the first generation of active microgels suffered from high opacity, which hindered live-cell imaging (Fig. 4a,b). Decreasing the nanoactuator concentration from 67 mg/ml to 12 mg/ml significantly improved the transparency of the gel, but notably reduced strain (Fig. 4c). The radial strain increased incrementally as nanoactuator concentration was increased, and visibility was drastically reduced above 24 mg/ml (Fig. 4c). An intermediate nanoactuator concentration of 18 mg/ml was selected for subsequent studies as a compromise. Further studies revealed that compressive strain was maximized at 7.1% surface DBCO modification, while higher degrees of surface functionalization led to nanoactuator agglomeration during microfluidic operation (Fig. 4d). Almost 50% of steady-state deformation was reached within 125 msec for optimized active microgels, while 1 sec of continuous exposure was required to achieve the maximum strain under the same illumination conditions (Fig. 4e).

Next, we characterized the deformation of single cell-laden microgels. The microtissues deformed with similar kinetics as the cell-free microactuators (Fig. 5a). The strain monotonically but very gradually increased, from 3.3±1.1% to 4.0±0.9%, with increasing pulse durations from 125 msec to 500 msec, respectively. Notably, powering the gels for 2000 msec significantly increased the maximum achievable radial strain to 4.7±1.3% (Fig. 5b). The actuation could be pulsed by modulating the frequency of laser illumination (Fig. S5), and raising the laser power from 30 mW to 50 mW increased the strain by 50%. Microgel actuation did not induce any detectable change in cell size (Fig. S5). Overall, this system is capable of applying the targeted strain levels, and allows the application of compressive strain over a large parameter matrix.

The rapid collapse of the microgels was enabled by heat generation due to the plasmon resonance effect of gold nanorods, and this may endanger cell viability. We studied heat transport in our system using two-dimensional finite element modelling. Computational results estimated a modest temperature increase at the interface where the cell resides (Fig. 5c). Consistent with these calculations, cell viability was not significantly affected following photothermal actuation with pulse durations less than 2000 msec (Fig. 5d, Fig. S5). Previous work has shown that gold nanorods heated with a laser power density of 11.3 μW μm^{-2} did not deteriorate cell viability *in* *vitro.*[23] We performed all experiments at 5.5 μW μm^{-2}, which is well below this power density level.

As a proof-of-concept demonstration, the active microgel platform was used to investigate MSC mechanobiology by monitoring changes in intracellular calcium intensity following isotropic compression. MSCs are well known for their sensitivity to cell-endogenous and exogenous forces, which impact various aspects of their biology including lineage commitment through mechanotransduction.[20,35-40] Calcium channel activation was selected as the mechanobiological response because ion channels such as PIEZO1, PIEZO2, and TRPV4 are known to be triggered via stretching, and in some cases by compression, in mammalian cells.[41-44] Indeed, single MSCs encapsulated within active microgels exhibited a significant change in intracellular calcium intensity when subjected to isotropic compression for 500 msec (Fig. 5e). The calcium spike reached a maximum intensity within 5.5 sec, and dissipated within half a minute (Fig. 5f). In order to verify whether the observed biological effect is due to mechanical compression, we encapsulated MSCs in control microgels which were capable of photothermal heating but incapable of generating compression due to the absence of click binding between alginate and the nanoactuators. MSCs encapsulated in control microgels with mechanically decoupled nanoactuators did not show any change in intracellular calcium intensity when subjected to the same level of laser power for the same duration (Fig. 5e, f). These findings were repeatable across multiple single cells encapsulated in active and control microgels (Fig. S5). Our findings are consistent with previous reports that showed uniaxial compression induces transient calcium signaling in MSCs within macroscale 3D scaffolds.[44,45]

Conclusions

We present a mechanically active cell culture platform for applications in mechanobiology. This system enables application of compressive strain on single cells in 3D culture conditions through optomechanical power transmission mechanism. Actuator performance is achieved with material design, and strains up to 15% and forces up to 400 nN can be generated. Optical actuation provides dynamic control over mechanical loading by regulating magnitude, duration, and frequency of compression. Isotropic compression is shown to induce transient calcium signaling in single MSCs.

This mechanically active cell culture system addresses the need for new approaches that bridge micromanipulation and cell supporting biomaterials. Moreover, the method can be extended to cell-cell mechanosignaling using multicellular active microgels, and can be adapted to monitor mechanosensitive downstream signaling events such as nuclear Yes-associated protein (YAP) translocation. Towards this goal, future work will focus on transitioning from strain controlled to force regulated microgels by experimentally measuring the generated stresses at the cell-biomaterial interface. Moreover, the influence of temperature changes on microgel elasticity will need to be investigated as thermoresponsive polymers can undergo significant stiffening when thermally activated which may simultaneously induce mechanobiological responses over long periods of actuation. The potential impact of photothermal heating on cell behavior must be studied in detail to discover and eliminate any off-target effects in order to maintain mechanical loading as the sole driver of the biological responses of interest. Future work will focus on studying MSC mechanobiology with this novel platform, particularly by investigating changes in focal adhesions, actin cytoskeleton, and nuclear shuttling of mechanosensitive transcription factors such as YAP. This mechanically active cell culture platform can be implemented with a variety of different mammalian cell types and has potential as a rapid biomechanical screening tool for large scale mechanobiology studies.

Experimental

Finite element models

All numerical simulations were conducted using finite element modeling software COMSOL Multiphysics 5.6 (COMSOL Inc.). Transient heat transfer simulations were performed with 15 vol% nanoactuator loading in a 35 μm sized microgel where cell diameter was selected as 20 μm. The nanoactuators were randomly distributed through the microshell in CAD drawings and the microgel was placed in a square bath, 500 μm by 500 μm. Laser illumination was assumed to provide uniform and constant heat generation which dissipated from the gold nanorods.[23] The thermal conductivity of the gold was 317 W mK^{-1} and the thermal conductivity as well as heat capacity of the gel network were assumed to be the same as water.[24] The absorption cross-section of gold nanorods was calculated as 10-16 m^2 using Radio Frequency module of COMSOL Multiphysics. Scattering field is defined based on the equations in reports by A. C. Polycarpou and S. Yushanov et al.[46,47] Frequency dependent refractive index of gold is taken from P. B. Johnson et al.[48] For the mesh, 0.15 μm minimum element size was used with a 1.3 element growth rate. A single laser pulse of 500 msec was applied at 5.5 μW μm^{-2} laser intensity and the cooling profile was observed for 1 sec while boundary bath temperature was set to 37°C. Numerical force simulations were performed based on our previous work. Isotropic compressive displacement was applied over the cell encapsulated microgel surface in 3D. Young's modulus of the cell was fixed at 3000 Pa[49] and a parametric sweep was performed for several Young's moduli of the microshell, ranging between 50-5000 Pa. For the mesh, 0.14 μm minimum element size with 1.4 element growth rate was used. Total force generated at cell-material interface was calculated by integrating calculated von-Misses stresses over the cell surface.

Nanoactuator fabrication

Nanoactuators were produced and characterized according to our previously reported work.[26] Gold nanorods were synthesized using a double surfactant (hexadecyltrimethylammonium bromide and sodium oleate) mediated wet chemistry process and were coated with pNIPMAM via *in situ* free radical polymerization.[23,26,50] The resulting nanoparticles were functionalized with DBCO (DBCO-NHS, Conju Probe) using amine-N-hydroxysuccinimide chemistry. The modification level was quantified via a fluorescence assay with azide-fluor 545 (Sigma Aldrich). The nanoactuators were imaged via transmission electron microscopy at 80 kV using negative staining. Hydrodynamic size and optical properties were measured using dynamic light scattering and UV-vis spectroscopy, respectively. The final nanoactuator solution was sterilized by freeze drying and resuspended in cell culture media at 5 mg ml^{-1} concentration by vigorous stirring overnight.

Alginate preparation and characterization

High molecular weight alginate (282 kDa) was purchased from KIMICA and was functionalized either with the integrin-binding peptide (Gly)4-Arg-Gly-Asp-Ser-Pro (GGGGRGDSP, Peptide 2.0) or with 11-azido-3,6,9-trioxaundecan-1-amine (Sigma Aldrich) via carboxiimide chemistry according to previously reported protocols.[15] Functionalized and unfunctionalized alginate were purified by dialysis, freeze dried, and stored under sterile conditions. The degree of RGD modification on alginate was measured by nuclear magnetic resonance (NMR, D2O, 500 MHz) spectroscopy using an internal standard method.[51] Potassium hydrogen phthalate (KHP) was chosen as the internal standard (δ at 7.50 ppm) and prepared in the same solution with the analytes at a constant concentration of 0.02 wt%. A standard calibration curve was first plotted using the integration ratio of 1H NMR peak area between 0.02 wt% KHP (δ at 7.50 ppm) and methylene units on the arginine of pristine RGD (varied from 0.03 wt% to 0.1 wt%, δ at 1.60 ppm). Next, RGD-modified alginate was dissolved at 1.5 wt% in D2O solvent containing 0.02 wt % of KHP. The concentration of RGD in the sample was quantified by correlating the integration ratio of 1H NMR peak area between KHP and conjugated RGD to the standard curve. The degree of RGD modification on alginate was calculated according to their mass fraction and molecular weight. On average, 9.4 RGD peptides were conjugated onto each alginate polymer. Azide functionalization was confirmed qualitatively using Fourier transform infrared spectroscopy (FTIR).

Microfluidic device fabrication and encapsulation

Microfluidic device fabrication and cell encapsulation were performed as described in our previous work with modifications.[15] Briefly, microfluidic devices were produced via polydimethylsiloxane based soft lithography and cell encapsulation was conducted using a mixture of alginates, nanoactuators, calcium carbonate, and cells at a flow rate of 1.5 µl min^{-1}. A mixture of Rhodamine-, azide-, and RGD-functionalized 2% alginate was mixed in 1:4:5 ratio prior to use. Concentrated nanoactuator solution at varying concentrations (12-36 mg/ml) was added to the alginate mixture and the solution was mixed vigorously prior to the addition of cells. Calcium carbonate nanoparticles ($CaCO_3$ NPs) were chosen as the crosslinker source. MSCs were incubated with 10 mg ml^{-1} $CaCO_3$ NPs for 5 minutes prior to encapsulation. The excess crosslinker source was removed by washing cells once with HEPES buffered cell culture media in order to maximize single cell encapsulation efficiency while minimizing the formation of empty microgels. All other reagent solutions were prepared directly with HEPES buffered cell culture media and the final pre-microgel mixture was injected through a two-channel device as demonstrated in prior work.[15]

Microscope platform

An inverted optical microscope (Olympus IX81) was retrofitted with a 785 nm laser (100 mW, Thorlabs), 4-channel fluorescence LED light source (Thorlabs), and an in-house built environmental chamber was used to perform actuation and live cell imaging simultaneously. Both the laser and the LED source were connected through the back port of the microscope using a dichroic mirror. The microscope, laser, and the fluorescence LED source were operated through the open-source software Micro-Manager. For this purpose, the laser controller (Thorlabs) was coupled to a function generator (Agilent) using an Arduino circuit board which provided computer control. All experiments unless otherwise stated were performed at 50 mW at 20X magnification corresponding to 5.5 µW µm^{-2} power density. Videos were captured at varying frame rates from 20 fps to 200 fps, depending on the experiment, and binning was used to improve fluorescence signal during intracellular calcium tracking. Active microgel deformation was determined using videos acquired under brightfield imaging during actuation and percentage radial strain was calculated using following equation,

$$\text{Radial strain (\%)} = (R_{off} - R_{on})/R_{off} * 100$$

where R_{off} refers to microgel radius prior to laser actuation and R_{on} refers to microgel radius during laser.

Cell culture and calcium assay

Murine MSCs (D1s, ATCC) were cultured in 10% fetal bovine serum containing high-glucose Dulbecco's Modified Eagle Serum (DMEM) with 1% penicillin/streptomycin at sub-confluency and used between passages 25-29. Viability of encapsulated MSCs was assessed using calcein-AM and ethidium homodimer-1 (Thermo Fisher, Invitrogen) at several time points before and 24 hours after microgel actuation. A live cell imaging compatible fluorescent dye (Calbryte 520 AM, AAT Bioquest) was used to track the intracellular calcium intensity of encapsulated MSCs in response to compression. MSC encapsulated microgels were incubated with 4.5 µM Calbryte in 310 mOsm isotonic solution for 45 minutes and used in compression experiments within 30 minutes.

Author Contributions

B. Ö., A. E.-A., and D. J. M. designed the study. B. Ö., J. L., C. M. T., and A. S. M. performed the experiments. B. Ö., M. S. S., and D. J. M. analyzed the data and wrote the manuscript with contributions from all authors.

Conflicts of interest

There are no conflicts to declare.

Acknowledgements

We gratefully acknowledge the support of the National Institutes of Health (NIH, 5R01DE013349), the National Science Foundation (NSF, MRSEC award DMR 14-20570). This work was supported by an NSF GRFP to CMT, and European Union's Horizon 2020 research and innovation programme under the Marie Sklodowska-Curie grant agreement No. 798504 (MECHANOSITY). We also thank Filiz Yeşilköy for her crucial contributions in numerical heat solutions and gratefully acknowledge Thomas Ferrante for his technical support in establishing the microscope platform.

References

1 X. Xu, J. Wang, L. Wu, J. Guo, Y. Song, T. Tian, W. Wang, Z. Zhu and C. Yang, *Small* 2020, **16**, 1–17.
2 Y. Deng, A. Finck and R. Fan, *Annu. Rev. Biomed. Eng.* 2019, **21**, 365–393.
3 A. P. Patel, I. Tirosh, J. J. Trombetta, A. K. Shalek, S. M. Gillespie, H. Wakimoto, D. P. Cahill, B. V. Nahed, W. T. Curry, R. L. Martuza, D. N. Louis, O. Rozenblatt-Rosen, M. L. Suvà, A. Regev and D. E. Bernstein, *Science* 2014, **344**, 1396–1402.
4 A. M. Klein, L. Mazutis, I. Akartuna, N. Tallapragada, A. Veres and V. Li, *Cell* 2015, **161**, 1187–1201.
5 R. M. Hochmuth, *J. Biomech.* 2000, **33**, 15–22.
6 H. Zhang and K. K. Liu, *J. R. Soc. Interface* 2008, **5**, 671–690.
7 N. Wang and D. E. Ingber, *Biochem. Cell Biol*. 1995, **73**, 327–335.
8 A. Elosegui-Artola, I. Andreu, A. E. Beedle, A. Lezamiz, M. Uroz, A. J. Kosmalska, R. Oria, J. Z. Kechagia, P. Rico-Lastres, A. L. Le Roux, C. M. Shanahan, X. Trepat, D. Navajas, S. Garcia-Manyes and P. Rosa-Cusachs, *Cell* 2017, **171**, 1397–1410.
9 M. J. Siedlik, V. D. Varner and C. M. Nelson, *Methods* 2016, **94**, 4–12.
10 D.-H. Kim, P. K. Wong, J. Park, A. Levchenko and Y. Sun, *Annu. Rev. Biomed. Eng.* 2009, **11**, 203–233.
11 E. M. Darling and D. Di Carlo, *Annu. Rev. Biomed. Eng.* 2015, **17**, 35–62.
12 F. Kurth, K. Eyer, A. Franco-Obregón and P. S. Dittrich, *Curr. Opin. Chem. Biol.* 2012, **16**, 400–408.
13 T. Rossow, P. S. Lienemann and D. J. Mooney, *Macromol. Chem. Phys.* 2016, **1600380**, 1–14.
14 D. Velasco, E. Tumarkin and E. Kumacheva, *Small* 2012, **8**, 1633–1642.
15 A. S. Mao, J.-W. Shin, S. Utech, H. Wang, O. Uzun, W. Li, M. Cooper, Y. Hu, L. Zhang, D. A. Weitz and D. J. Mooney, *Nat. Mater.* 2017, **16**, 236–243.
16 A. S. Mao, B. Özkale, N. J. Shah, K. H. Vining, T. Descombes, L. Zhang, C. M. Tringides, S.-W. Wong, J.-W. Shin, D. T. Scadden, D. A. Weitz and D. J. Mooney, *Proc. Natl. Acad. Sci.* 2019, **116**, 15392–15397.
17 K. Y. Lee and D. J. Mooney, *Prog. Polym. Sci.* 2013, **37**, 106–126.
18 E. Ruvinov and S. Cohen, *Adv. Drug Deliv. Rev.* 2016, **96**, 54–76.
19 E. R. West, M. Xu, T. K. Woodruf and L. D. Shea, *Biomaterials*, 2007, **28**, 4439–4448.
20 N. Huebsch, P.R. Arany, A. S. Mao, D. Shvartsman, O. A. Ali, S. A. Bencherif, J. Rivera-Feliciano and D. J. Mooney, *Nat. Mater.* 2010, **9**, 518–526.
21 O. Chaudhuri, S. T. Koshy, C. B. Da Cunha, J.-W. Shin, C. S. Verbeke, K. H. Allison and D. J. Mooney, *Nat. Mater.* 2014, **13**, 1–35.
22 D.-H. Kim, P. K. Wong, J. Park, A. Levchenko, Y. Sun, *Annu. Rev. Biomed. Eng.* 2009, **11**, 203-233.
23 Z. Liu, Y. Liu, Y. Chang, H. R. Seyf, A. Henry, A. L. Mattheyses, K. Yehl, Y. Zhang, Z. Huang and K. Salaita, *Nat. Methods* 2016, **13**, 143–146.
24 A. Sutton, T. Shirman, J. V. I. Timonen, G. T. England, P. Kim, M. Kolle, T. Ferrante, L. D. Zarzar, E. Strong and J. Aizenberg, *Nat. Commun.* 2017, **8**, 14700.
25 M. Monticelli, D. S. Jokhun, D. Petti, G. V. Shivashankar, R. Bertacco, *Lab Chip*, 2018, **18**, 2955-2965.
26 B. Özkale, R. Parreira, A. Bekdemir, L. Pancaldi, E. Özelçi, C. Amadio, M. Kaynak, F. Stellacci, D. J. Mooney and M. S. Sakar, *Lab Chip* 2019, **19**, 778–788.
27 R. Parreira, E. Özelçi and M. S. Sakar, *Front. Robot. AI* 2021, **8**, 649765.
28 F. E. Uslu, C. D. Davidson, E. Mailand, N. Bouklas, B. M. Baker and M. S. Sakar, *Adv. Mater.* 2021, **33**, 2102641.
29 D. O. Asgeirsson, M. G. Christiansen, T. Valentin, L. Somm, N. Mirkhani, A. H. Nami, V. Hosseini and S. Schuerle, *Lab Chip* 2021, **21**, 3850–3862.
30 X. Zhao, N. Huebsch, D. J. Mooney and Z. Suo, *J. Appl. Phys.* 2010, **107**, 063509.
31 G.L. Puleo, F. Zulli, M. Piovanelli, M. Giordano, B. Mazzolai, L. Beccai and L. Andreozzi, *React. Func. Polym.* 2013, **73**, 1306-1318
32 M.A. Haq, Y. Su and D. Wang, *Mater Sci. Engg.* 2017, **70**, 842-855.
33 B. Özkale, M. S. Sakar and D. J. Mooney, *Biomaterials* 2021, **267**, 120497.
34 M. Das, N. Sanson, D. Fava and E. Kumacheva, *Langmuir* 2007, **23**, 196-201.
35 J. Zhang, C. Cheng, J. L. Cuellar-Camacho, M. Li, Y. Xia, W. Li and R. Haag, *Adv. Funct. Mater.* 2018, **28**, 1–12.
36 R. K. Das, V. Gocheva, R. Hammink, O. F. Zouani and A. E. Rowan, *Nat. Mater.* 2016, **15**, 318–325.
37 A. J. Engler, S. Sen, H. L. Sweeney and D. E. Discher, *Cell* 2006, **126**, 677–689.
38 B. D. Cosgrove, K. L. Mui, T. P. Driscoll, S. R. Caliari, K. D. Mehta, R. K. Assoian, J. A. Burdick and R. L. Mauck, *Nat. Mater.* 2016, **15**, 1297–1306.
39 S. D. Subramony, B. R. Dargis, M. Castillo, E. U. Azeloglu, M. S. Tracey, A. Su and H- H. Lu, *Biomaterials* 2013, **34**, 1942–1953.
40 M. M. Pathak, J. L. Nourse, T. Tran, J. Hwe, J. Arulmoli, D. T. T. Le, E. Bernardis, L. A. Flanagan and F. Tombola, *Proc. Natl. Acad. Sci.* 2014, **111**, 16148–16153.
41 C. Pardo-Pastor, F. Rubio-Moscardoa, M. Vogel-González, S. A. Serra, A. Afthinos, S. Mrkonjic, O. Destaing, J. F. Abenza, J. M. Fernández-Fernández, X. Trepat, C. Albiges-Rizo, K. Konstantopoulos and M. A. Valverde, *Proc. Natl. Acad. Sci.* 2018, **115**, 1925–1930.
42 S. A. Gudipaty, J. Lindblom, P. D. Loftus, J. Redd, K. Edes, F. Davey, V. Krishnegowda and J. Rosenblatt, *Nature* 2017, **543**, 118–121.
43 L. He, J. Tao, D. Maity, F. Si, Y. Wu, T. Wu, V. Prasath, D. Wirtz and S. X. Sun, *J. Cell Sci.* 2018, **131**, jcs208470.
44 J. J. Campbell, D. L. Bader and D. A. Lee, *J. Appl. Biomater.* 2008, **6**, 9–15.
45 L. A. McMahon, V. A. Campbell and P. J. Prendergast, *J. Biomech.*, 2008, **41**, 2055–2059.

46 A. C. Polycarpou, *Synth. Lect. Comput. Electromagn.*, 2006, **1**, 1–126.
47 S. Yushanov, J. S. Crompton and K. C. Koppenhoefer, presented at *Proc. 2013 COMSOL Conf.* Boston, 2013.
48 P. B. Johnson and R. W. Christy, *Phys. Rev. B* 1972, **6**, 4370–4379.
49 I. Titushkin and M. Cho, *Biophys. J.* 2007, **93**, 3693–3702.
50 X. Ye, C. Zheng, J. Chen, Y. Gao and C. B. Murray, *Nano Lett.* 2013, **13**, 765–771.
51 S. Nam, R. Stowers, J. Lou, Y. Xia and O. Chaudhuri, *Biomaterials* 2019, **200**, 15–24.